Journal of the European Ceramic Society 44 (2024) 215–223

Contents lists available at ScienceDirect

Journal of the European Ceramic Society

journal homepage: www.elsevier.com/locate/jeurceramsoc

Highly compatible and reliable ZrN interfacial layer between TiN top electrode and antiferroelectric ZrO_2 thin film to boost the electrocaloric behavior

Yu-Hua Liu [a], Han-Hsiang Tai [a], Chi-An Ho [a], Ting-Han Lin [b], Ming-Chung Wu [b,c,d], Jer-Chyi Wang [a,c,e,f,*]

[a] Department of Electronic Engineering, Chang Gung University, Guishan Dist., 33302 Taoyuan, Taiwan
[b] Department of Chemical and Materials Engineering, Chang Gung University, Guishan Dist., 33302 Taoyuan, Taiwan
[c] Green Technology Research Center, Chang Gung University, Guishan Dist., 33302 Taoyuan, Taiwan
[d] Division of Neonatology, Department of Pediatrics, Chang Gung Memorial Hospital, Linkou, Guishan Dist., 33305 Taoyuan, Taiwan
[e] Department of Neurosurgery, Chang Gung Memorial Hospital, Linkou, Guishan Dist., 33305 Taoyuan, Taiwan
[f] Department of Electronic Engineering, Ming Chi University of Technology, Taishan Dist., 243303 New Taipei City, Taiwan

ARTICLE INFO

Keywords:
Antiferroelectric (AFE)
Electrocaloric (EC)
Zirconium nitride (ZrN)
Zirconia (ZrO_2)
Atomic layer deposition (ALD)

ABSTRACT

A highly compatible and reliable ZrN interfacial layer with different cycles of atomic layer deposition was inserted between the TiN top electrode and antiferroelectric (AFE) ZrO_2 thin film to achieve low oxygen vacancies and high crystallinity of the ZrO_2 thin film, boosting the AFE and electrocaloric (EC) characteristics of TiN/ZrO_2/TiN metal–insulator–metal (MIM) capacitors. An outstanding adiabatic temperature change (ΔT) of −21 K was realized for devices with a ZrN interfacial layer of nine cycles, which can be ascribed to the reduction in redox between the TiN and ZrO_2 for the suppression of interfacial dead layer during annealing as confirmed via high-angle annular dark field images and interfacial capacitance measurement. Hence, the reliability of ZrO_2 MIM capacitors with a nine-cycle ZrN interfacial layer was examined with a negligible change in AFE and EC behaviors after a cycling endurance test of 10^6 cycles, exhibiting great potential for future applications in solid-state cooling.

1. Introduction

With a rapid development of electronics industry to explore a metaverse, the high-density integrated circuits (ICs) with a fast clock rate are inevitable and often accompanied by a severe thermal design power (TDP) [1]. It is predicted that the TDP of high-performance graphic processing units (GPUs) will reach at least 700 watts before 2025 [2]. Hence, the demand for efficient cooling systems in ICs has increased urgently. However, the application of traditional cooling fan and heat sink in ICs encounters some bottlenecks such as the low efficiency, scaling limitation, and environmental pollutions [3]. Thus, some techniques using the electrocaloric (EC) effect, pyroelectric effect, or magnetocaloric effect have been proposed for the next-generation cooling in ICs. Among them, EC effect has been considered as the most promising method because of its mature manufacturing in complementary metal-oxide-semiconductor (CMOS), good scalability, and simple operation [4]. Electrocaloricity is a phenomenon which can be defined as the adiabatic temperature change (ΔT) induced by applying or removing an external electric field in dielectric materials with the polarized behaviors [5]. When an external electric field is applied on the dielectric material, the originally chaotic dipole will be aligned with the direction of the field. In an adiabatic system, to compensate the entropy disturbance caused by the polarization, the material would generate additional entropy as offset, which would be manifested in the form of temperature to warm up or cool down the system [6]. The ΔT can be quantified as a temperature change with the electric field and directly measured via the thermal microscopy, thermocouples, and infrared camera [7]. Besides, it can be indirectly extracted from the polarization versus temperature curves under different electric fields by using Maxwell's equations [8].

Additionally, the EC effect has been reported in various dielectric materials, including polymers, perovskite ceramics, and high dielectric

* Correspondence to: Department of Electronic Engineering, Chang Gung University, 259 Wen-Hwa 1st Road, Guishan Dist., 33302 Taoyuan, Taiwan.
E-mail address: jcwang@mail.cgu.edu.tw (J.-C. Wang).

https://doi.org/10.1016/j.jeurceramsoc.2023.08.051
Received 27 April 2023; Received in revised form 1 August 2023; Accepted 27 August 2023
Available online 28 August 2023

constant (high-k) ceramic thin films [9–11]. Among these materials, a large ΔT has been achieved in ferroelectric hafnium zirconium oxide (HZO) and antiferroelectric (AFE) ZrO_2 thin films via an atomic layer deposition (ALD) system with a simple process, high scalability, and robust reliability [12,13]. Compared to ferroelectric materials, the AFE materials exhibit double polarized hysteresis loops with zero remnant polarization at zero bias, which can be ascribed to the field-induced phase transition between the non-polar tetragonal phase to the polar orthorhombic phase [14]. Therefore, AFE materials can demonstrate stable polarization switching and high fatigue resistance due to their relatively small depolarization field, suitable for the EC application in ICs [15]. Nevertheless, there are still some issues at the interface between the high-k ceramic layer and metal electrode such as the redistribution of oxygen vacancy, electrode oxidation, and plasma damage, leading to the extra defects and unwanted interfacial layer for the degraded polarization and EC characteristics [16,17]. Previously, methods have been proposed to solve the interfacial problems at bottom electrode (BE) interface of ferroelectric HZO capacitors, which are originated from the oxidation of TiN during the ALD deposition. HfN and in-situ TiN have been inserted between HZO and TiN layers, giving rise to the inhibition in the formation of interfacial TiO_x dead layer [18]. Additionally, Chen et al. presented that the redistribution of oxygen vacancy at the interface can be effectively suppressed via the NH_3 plasma surface treatment [19]. Thus far, these technologies have been applied at the BE interface of ferroelectric HZO capacitors to improve their memory characteristics. In this study, the enhancement of AFE and EC behaviors in TiN/ZrO_2/TiN metal–insulator–metal (MIM) capacitors via the interfacial zirconium nitride (ZrN) passivation at the top electrode (TE) interface has been proposed, which is relatively more compatible for the ZrO_2 thin films and has not yet been discussed before. ZrN has excellent corrosion and oxidation resistance properties, which has been used as diffusion barriers [20,21], oxygen reduction catalysts [22], and biomedical coatings [23,24]. Here, the influence of a ZrN interfacial layer with different ALD cycles on the redox reaction between the TiN and ZrO_2 during the annealing process as well as the AFE and EC characteristics and reliabilities of the AFE ZrO_2 thin film was investigated. The enhanced behaviors of the TiN/ZrO_2/TiN MIM capacitors with a ZrN interfacial layer can be ascribed to the thin interfacial dead layer, resulted from the less redox reaction. Furthermore, the robust reliability under the cycling endurance tests was realized because of the suppression of the oxygen vacancy generation during the cycling operation.

2. Experimental

2.1. Sample preparation

The AFE ZrO_2 capacitors with a ZrN interfacial layer were fabricated on 4-inch n^+-silicon wafers. After the removal of the native oxide using a diluted HF solution, a 100-nm-thick TiN film was deposited via a dc sputtering system (G3.5 Cluster, FSE Corp., New Taipei City, Taiwan) at 5 kW as the bottom electrode (BE). The gas flow rates of argon and nitrogen were kept at 30 and 30 sccm, respectively, to maintain a working pressure of 3 mTorr. Then, a 10-nm-thick ZrO_2 layer was deposited via a plasma-enhanced ALD (PEALD) system (Cambridge NanoTech Fiji-202 DCS, Oxford instruments, Oxford, UK) at 250 °C. Subsequently, a ZrN interfacial layer with different ALD cycles of 3, 6, 9, and 12 were deposited on the ZrO_2 layer and denoted as ZrN_3, ZrN_6, ZrN_9, and ZrN_12, respectively. A reference device without a ZrN interfacial layer was also prepared and denoted as w/o. For the deposition of ZrO_2 and ZrN layers, tetrakis(dimethylamino) zirconium (TDMAZ), O_2 plasma, and NH_3 plasma were used as the precursors of Zr, O, and N, respectively. After that, a 100-nm-thick TiN film was deposited on all devices as the top electrode (TE) and then annealed at 600 °C for 30 s in N_2 ambient (AccuThermo AW 810 RTP, Allwin21 Corp., Morgan Hill, CA, USA) to form the AFE phase of the ZrO_2 thin films. Finally, the TE was patterned via photolithography and then etched using a NH_4OH:H_2O_2:H_2O (1:1:5) solution to obtain the isolated electrodes with a diameter of 100 μm.

2.2. Characterization of materials and devices

The chemical composition at the interface between the TiN TE and ZrO_2 thin film was analyzed using X-ray photoelectron spectroscopy (XPS) (Theta Probe ARXPS, Waltham, KS, USA) at 10^{-9} Torr with Al Kα as the X-ray source (1486.7 eV). Furthermore, the crystallization behaviors of ZrO_2 thin films were confirmed via grazing incidence X-ray diffraction (GIXRD) (X'Pert Pro MRD, Almelo, Netherlands) with Cu Kα radiation ($\lambda = 0.154$ nm) at an incident angle of 0.5° and high-resolution transmission electron microscope (HRTEM) (JEM-2100PLUS, JEOL, Tokyo, Japan). To investigate the polarized phases of the TiN/ZrO_2/TiN stacked films with a ZrN interfacial layer, high-angle annular dark field (HAADF) images were obtained via spherical-aberration corrected field emission TEM (JEM-ARM200FTH, JEOL, Tokyo, Japan) at an accelerating voltage of 200 kV. The dark-field lattice images have a resolution of 0.08 nm. For the AFE and EC behaviors, the current density versus electric field (J—E) and the polarization versus electric field (P—E) curves of the TiN/ZrO_2/TiN MIM capacitors with a ZrN interfacial layer were performed using a Keithley 4200-SCS semiconductor analyzer equipped with a 4225-PMU ultrafast IV unit (Tektronix, Inc., Beaverton, OR, USA). A triangular bipolar voltage pulse with a rising and falling time of 50 μs was applied to the top electrode of the AFE ZrO_2 capacitors with a ZrN interfacial layer. Meanwhile, the bottom electrode was definitely grounded.

3. Results and discussion

3.1. Material analyses of TiN/ZrN/ZrO_2/TiN stacked structures

Figs. 1a and S1 show the XPS depth profiles of atomic percentages of Ti, N, Zr, and O atoms for the TiN/ZrO_2/TiN stacked structures without and with a ZrN interfacial layer at TiN TE and ZrO_2 interface respectively. From these figures, it can be found that the percentage of oxygen atoms in ZrO_2 thin films became higher with an increase in ALD cycles of the ZrN interfacial layer. Furthermore, the interface between the TiN TE and ZrO_2 thin film was identified to be at the position under an Ar sputtering of approximately 2600 s. Therefore, the O 1 *s* XPS spectra of the TiN/ZrO_2/TiN stacked structures with different ZrN cycles at the TiN TE and ZrO_2 interface to the middle of ZrO_2 thin films under different Ar sputtering times were investigated and are shown in Figs. 1b and S2a-d respectively. All the spectra can be deconvoluted into three primary peaks: the Zr-O bond at 531.3 eV [25], the Ti-O bond at 530 eV [25], and the non-lattice oxygen at 533.8 eV [26,27]. When the ALD cycles of the ZrN layer increased, the intensities of Ti-O bond reduced owing to the suppression of the interaction between TiN TE and ZrO_2 thin films during the annealing process. Moreover, the peak-to-area ratios (PARs) of Ti-O bond at the TiN TE and ZrO_2 interface to the middle of ZrO_2 thin films under different Ar sputtering times were calculated with respect to the total amount of XPS peak areas and are illustrated in Fig. 1c. The quantified results indicate that the oxidation of TiN TE can be effectively inhibited via the ZrN interfacial layer. The phenomenon can be further confirmed by the Ti 2*p* XPS spectra (Fig. S3), where Ti-O bonds have been identified at 463 eV ($2p_{1/2}$) and 456.8 eV ($2p_{3/2}$) [28], Ti-N bonds have been determined at 460.8 eV ($2p_{1/2}$) and 455.6 eV ($2p_{3/2}$) [29], and the non-lattice titanium have been detected at 458.4 eV ($2p_{1/2}$) and 454.7 eV ($2p_{3/2}$) [30]. Fig. 1d shows the Zr 3*d* XPS spectra of the samples with different ZrN cycles at the interface between the TiN TE and ZrO_2 thin films. The spectra can be deconvoluted into three peaks, including Zr-O bonds at 185.3 eV ($3d_{3/2}$) and 183.1 eV ($3d_{5/2}$) [31], Zr-N bonds at 182.2 eV ($3d_{3/2}$) and 180.9 eV ($3d_{5/2}$) [32,33], and the non-lattice zirconium at 181.7 eV ($3d_{3/2}$) and 179.1 eV ($3d_{5/2}$) [34]. Obviously, the peak intensity of Zr-N bonds increased with an increase in ALD cycles of

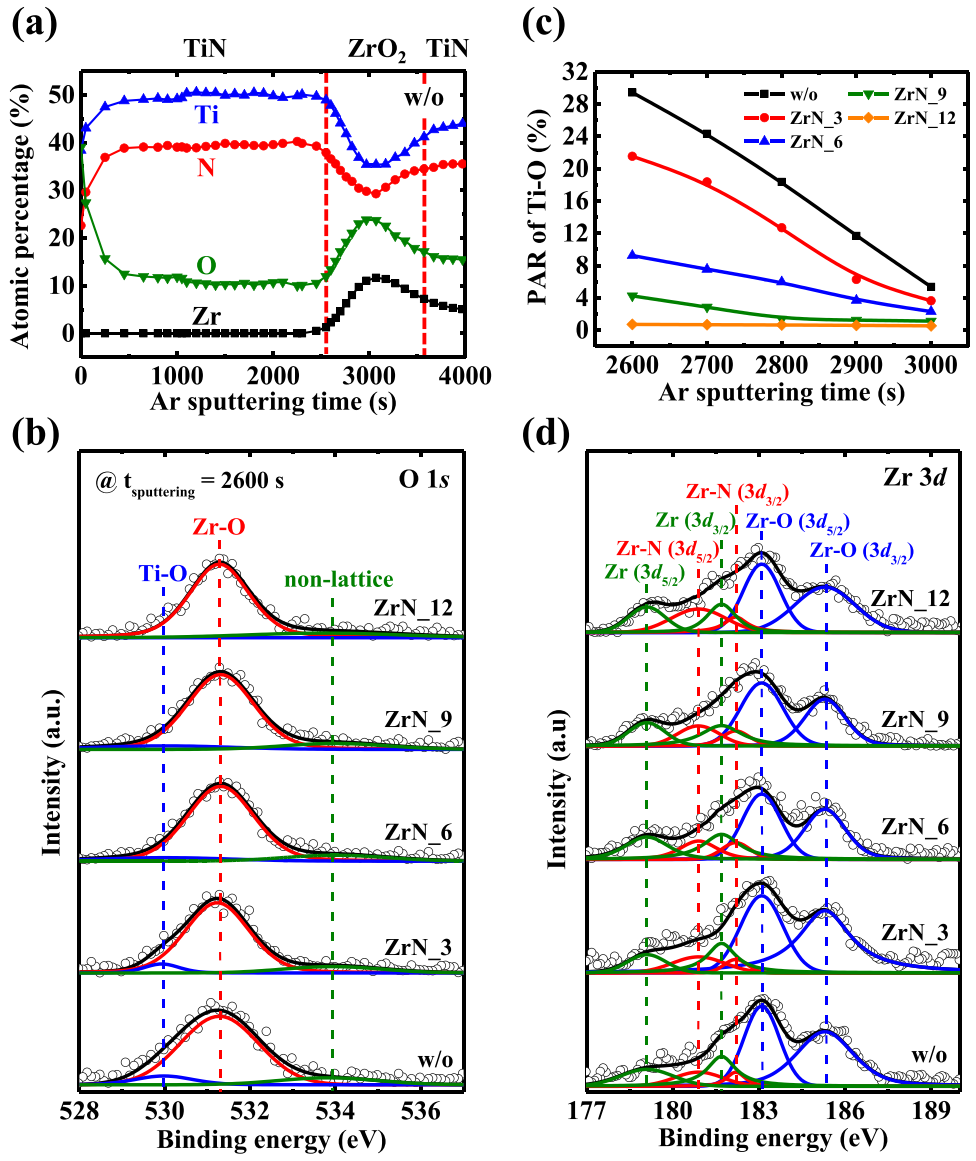

Fig. 1. (a) XPS depth profile of TiN/ZrO_2/TiN stacked films without a ZrN interfacial layer. (b) O 1 *s* and (d) Zr 3*d* XPS spectra of TiN/ZrO_2/TiN stacked films with different ALD cycles of ZrN interfacial layers under a 2600-s Ar sputtering time. (c) XPS PAR of Ti-O bond of TiN/ZrO_2/TiN stacked films with different ALD cycles of ZrN interfacial layers under different Ar sputtering times.

the ZrN interfacial layer for the oxidation inhibition of TiN TE.

Fig. 2a shows the GIXRD diffractograms of the TiN/ZrO_2/TiN stacked films with different ZrN cycles at the TiN TE and ZrO_2 interface. According to the diffraction powder data [35], the diffraction peaks, located at 37°, 42.68°, and 61.93° can be identified as the crystallinity of TiN films. Additionally, the peaks located at 30.27°, 35.26°, 50.37°, 59.61°, 60.21°, and 74.54° represent the t(011), t(110), t(112), t(013), t(121), and t(220) peaks of zirconia, respectively, corresponding to the AFE behaviors of ZrO_2 thin films [36]. To further analyze the crystalline structure of the stacked films with different ZrN cycles, the GIXRD spectra in the 2θ range of 27–34° were magnified and are presented in Fig. 2b. In these spectra, the ZrN_9 sample exhibits the highest intensity of t(011) peak. The enhanced crystallinity of ZrO_2 thin films with a ZrN interfacial layer between TiN TE and ZrO_2 can be ascribed to the reduction in interfacial dead layer [37]. Nevertheless, for the ZrN_12 sample, a lower intensity of t(011) peak was observed as compared with that of the ZrN_9, implying the deficient crystallinity of the tetragonal phase in ZrO_2 thin films owing to the additional stress induced by the thick ZrN interfacial layer [38]. Furthermore, the grain sizes of all samples were extracted to confirm the effectiveness of ZrN interfacial layer on crystallization of ZrO_2 thin films based on Scherrer equation [39]:

$$\tau = \frac{k\lambda}{\beta \times \cos\theta} \quad (1)$$

where τ is the mean size of the crystalline domains, i.e. the grain size of ZrO_2 thin films, k is the dimensionless shape factor close to unity, λ is the X-ray wavelength of 0.154 nm, β is the full width at half maximum (FWHM) of the peak, and θ is the Bragg angle of 30.27°. Fig. 2c presents the calculated grain sizes of the TiN/ZrO_2/TiN stacked films with different ZrN cycles at the TiN TE and ZrO_2 interface. The grain size of the ZrN_9 sample was close to the film thickness of 10 nm, indicating a complete crystallization of the ZrO_2 thin film. Fig. 3a,b and Fig. S4a show the cross-sectional HRTEM images of the TiN/ZrO_2/TiN stacked films without and with a ZrN interfacial layer of 9 and 12 cycles, respectively, to visually confirm the crystallinity. Moreover, the crystallinity of the stacked films was further quantified via HAADF imaging, as shown in Fig. 3c,d and Fig. S4b. The bottom figures show the high-magnification images of the lattice with the corresponding fast Fourier

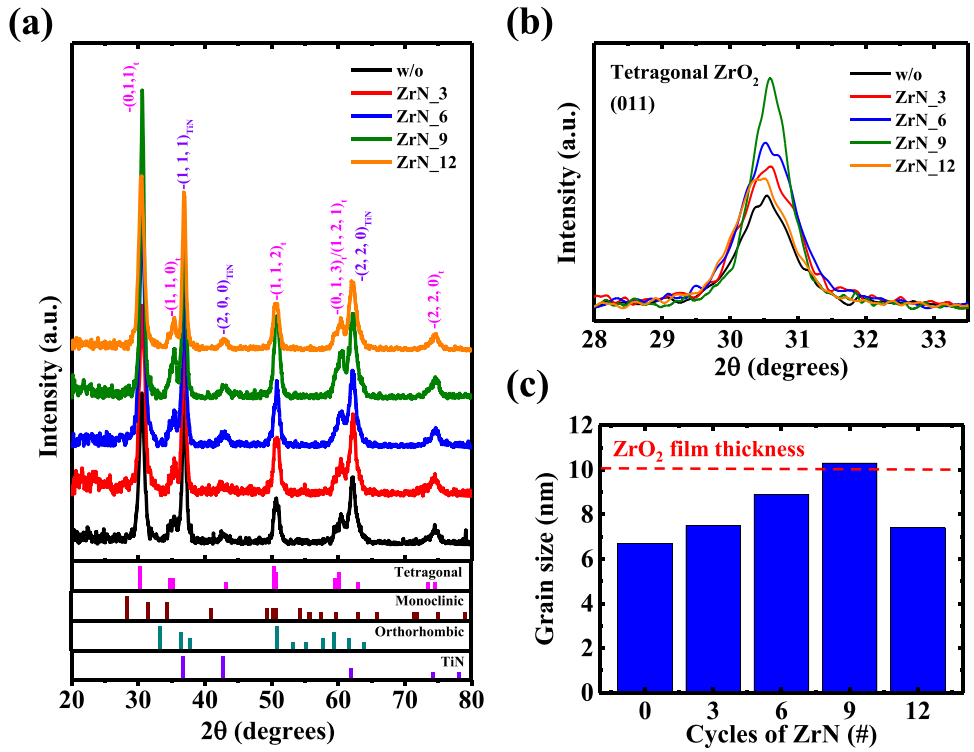

Fig. 2. (a) GIXRD patterns and (b) magnified spectra in the 2θ range of 27–34° (tetragonal 011) of TiN/ZrO_2/TiN stacked films with different ALD cycles of ZrN interfacial layers. The reference numbers of powder diffraction files are TiN (cubic): 01-087-0632, ZrO_2 (tetragonal): 00-050-1089, ZrO_2 (monoclinic): 01-074-1200, and ZrO_2 (orthorhombic): 00-034-1084. (c) Calculated grain sizes of ZrO_2 film films with different ALD cycles of ZrN interfacial layers.

transformed patterns and the simulated atomic columns confirming the tetragonal phase for the matrix. By examining these images, we can observe the highly ordered arrangement of Zr atoms in the ZrN_9 sample, indicating that the optimal cyclic deposition of ZrN interfacial layer can improve the crystallinity of ZrO_2 thin films, corresponding to the calculated grain sizes in Fig. 2c. The enhanced tetragonal phase at the TiN TE and ZrO_2 interface can be attributed to the thinner interfacial dead layer, effectively stabilizing the crystallinity of tetragonal phase at the interface to achieve a large grain. Additionally, the film thickness extracted from the HRTEM images can be used to calculate the electric field of ZrO_2 thin films for further characterizations of AFE and EC behaviors.

3.2. Antiferroelectric behaviors of TiN/ZrN/ZrO_2/TiN capacitors

To investigate the effects of the ZrN interfacial layer on the AFE characteristics of TiN/ZrO_2/TiN MIM capacitors, the *J*—*E* and *P*—*E* hysteresis curves were measured using the triangular bipolar pulses with rising and falling times of 50 μs and are shown in Fig. 4a and b, respectively. According to the film thicknesses obtained from the HRTEM images, the voltages of 5, 5.15, 5.3, 5.45, and 5.6 V, respectively, were applied to w/o, ZrN_3, ZrN_6, ZrN_9, and ZrN_12 samples to get the same electric field of 5 MV/cm. In this figure, the ZrN_9 sample exhibited the largest polarization of 41.3 μC/cm^2, corresponding to a more complete crystallization in ZrO_2 thin films, as shown in Fig. 3. Additionally, the critical electric field of the ZrN_9 sample was observed to be significantly reduced. The enhanced AFE behaviors could be attributed to the huge amount of polarized domains in ZrO_2 thin films with a ZrN interfacial layer of 9 cycles [40]. However, the polarization of ZrO_2 thin films with a ZrN interfacial layer of 12 cycles declined obviously. To identify if the polarization can be further enhanced, a larger electric field of 6 MV/cm was applied on the ZrN_12 sample, as shown in Fig. S5. It can be observed that even at a higher electric field, the ZrN_12 sample exhibited a smaller P_s than that of the ZrN_9, indicating a poor crystallinity of ZrO_2 thin films as revealed in Figs. 2 and 3. Fig. 4c shows the energy storage properties of the TiN/ZrO_2/TiN MIM capacitors with different cycles of ZrN layers at the TiN TE and ZrO_2 interface, where the energy storage density (ESD) and energy loss can be obtained via the integral of the blue and orange areas of the *P*—*E* hysteresis curves, as illustrated in the inset of Fig. 4b. Furthermore, the efficiency can be calculated based on the following equation:

$$\text{Efficiency} = \frac{\text{ESD}}{\text{ESD} + \text{loss}} \quad (2)$$

The ESD and efficiency of the ZrN_9 sample were significantly enhanced to 80.2 J/cm^3 and 64.2 % respectively, suitable for applications in supercapacitors [41], as confirmed by the high dielectric permittivity in the permittivity versus electric field (ε—*E*) characteristics (Fig. S6). Furthermore, the ESD and efficiency of the samples as a function of the operation frequency was investigated and is shown in Fig. S7. Too high and low frequency operations would degrade the energy storage performance of AFE ZrO_2 thin films because the polarization is screened by the RC delay and leakage current, respectively [42,43]. Fig. 4d shows the cycling endurance characteristics of the devices stressed at 5 MV/cm with the pulse width of 50 μs for 10^6 cycles to further validate that the ZrN interfacial layer can improve not only the polarization but also reliability behaviors of the TiN/ZrO_2/TiN stacked films. The *P*—*E* hysteresis curves of all samples after different numbers of cycling pulses are shown in Fig. S8. When the ALD cycles of ZrN deposition increased, the change in ESD and efficiency of TiN/ZrO_2/TiN MIM capacitors after 10^6 cycling pulses was reduced significantly. It is reported that the degradation of high-k FE and AFE materials after cycling endurance tests was highly correlated with the defects in dielectric thin films [44]. For the devices with a ZrN interfacial layer, the additional nitrogen in ZrN layers can effectively reduce the generation of oxygen vacancies at the TiN TE and ZrO_2 interface during the cycling operations [45,46], enhancing the cycling endurance stability of the TiN/ZrO_2/TiN MIM capacitors.

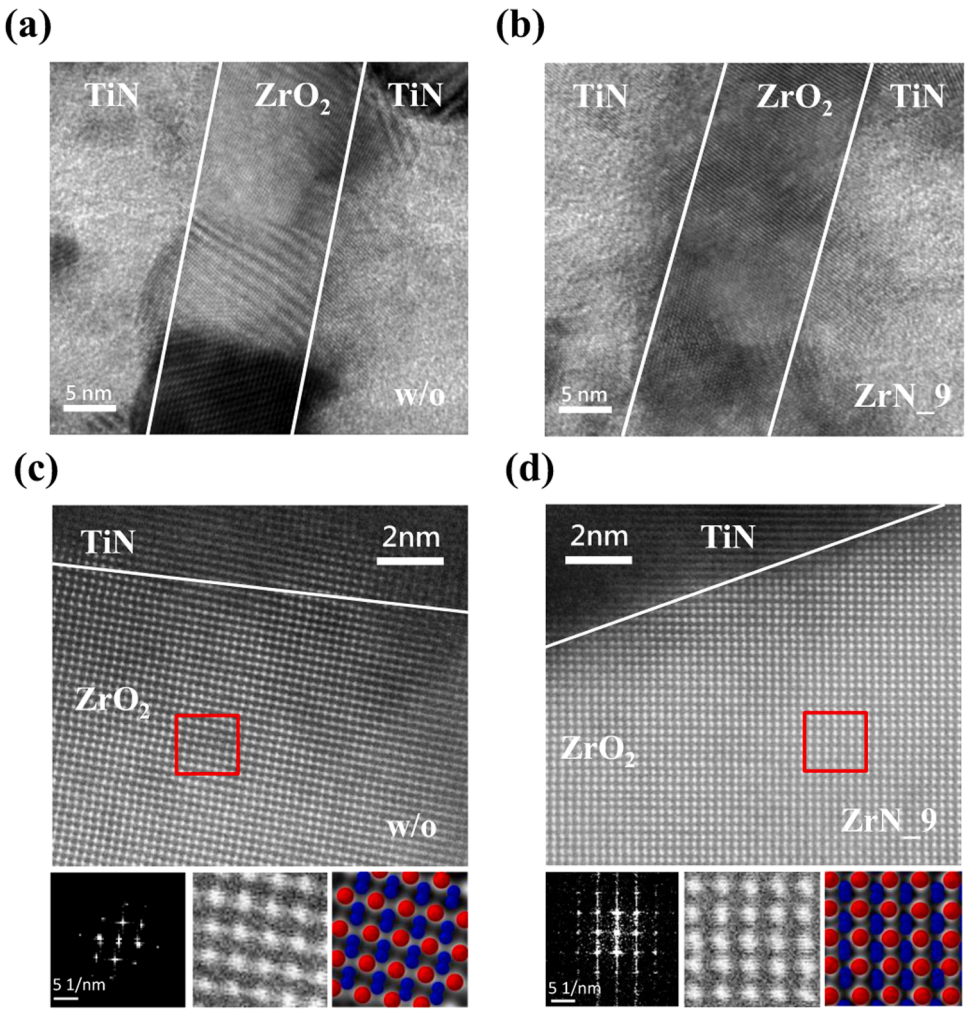

Fig. 3. HRTEM images of TiN/ZrO_2/TiN stacked films (a) without and (b) with a ZrN interfacial layer of 9 cycles. HAADF micrographs of TiN/ZrO_2/TiN stacked films (c) without and (d) with a ZrN interfacial layer of 9 cycles. The bottom figures in (c) and (d) show the high-magnification images of the lattice with the corresponding fast Fourier transformed patterns and the atomic simulation for the tetragonal phase with Zr columns in red and O columns in blue.

In addition to the materials analysis, the pulse switching measurement has been applied to analyze the interface between the FE/AFE films and the metal electrode quantitatively, as proposed by Park et al. [47]. The polarization switching kinetics could be strongly affected by the properties of the interfacial capacitance (C_i) originated from the non-polarized layer at the interface [18]. Fig. 5a and b shows the switching current versus time ($I_{sw}-t$) characteristics of the TiN/ZrO$_2$/TiN MIM capacitors without and with a ZrN interfacial layer of 9 cycles, respectively. The waveform of voltage applied to the samples during measurement was illustrated in Fig. S9. The C_i can be extracted from the region 2 of the waveform, representing the switching current of the process from non-polar to polar phases. According to the polarization reversal theory, the switching current can be described as follows [47,48]:

$$I_{sw}(t) = I_{sw}^{0} e^{\frac{t-t_0}{R_L C_i}} \quad (t_0 \le t \le t_{sw}) \tag{3}$$

where t_0 and t_{sw} are the times when the film starts switching and when the switching is finished, respectively, and R_L is the total resistance of the measurement system. Additionally, I_{sw}^{0} is the current in the beginning of the polarization switching, which was indicated by the black arrow in these figures and can be expressed as follows:

$$I_{sw}^{0} = \frac{(E_a - E_c)t_f}{R_L} \tag{4}$$

where E_a, E_c, and t_f are the applied electric field, the coercive field, and the thickness of ZrO_2 thin films, respectively. R_L and E_c can be extracted from the slope and the intercept of x-axis in I_{sw}^{0} versus E_a characteristics, respectively, as shown in the inset of Fig. 5a and b. Thus, the C_i can be obtained by substituting the calculated value of R_L into Eq. (3). Thanks to the modification of the interface between the ZrO_2 thin film and TiN electrode, the C_i of the ZrN_9 sample was 43.3 μF/cm^2, approximately 5.5 times higher than that of the sample without a ZrN interfacial layer, implying that the formation of the interfacial dead layer can be effectively suppressed by the ZrN interfacial layer. To show the improvement intuitively, the schematics of the interface between the ZrO_2 thin films and TiN electrode of the samples without and with a ZrN interfacial layer of 9 cycles are illustrated in Fig. 5c and d, respectively. For the sample without a ZrN interfacial layer, the oxidation of the TiN electrode would occur during the annealing process, causing a thicker interfacial dead layer and fewer domains for the polarization. On the other hand, the ZrN interfacial layer can suppress the reaction between the ZrO_2 thin films and TiN electrode effectively, leading to the improved interface quality and enhanced crystallinity of the ZrO_2 thin films.

3.3. Electrocaloric effects of TiN/ZrN/ZrO$_2$/TiN capacitors

To investigate the EC effect, the $P-E$ hysteresis curves of the

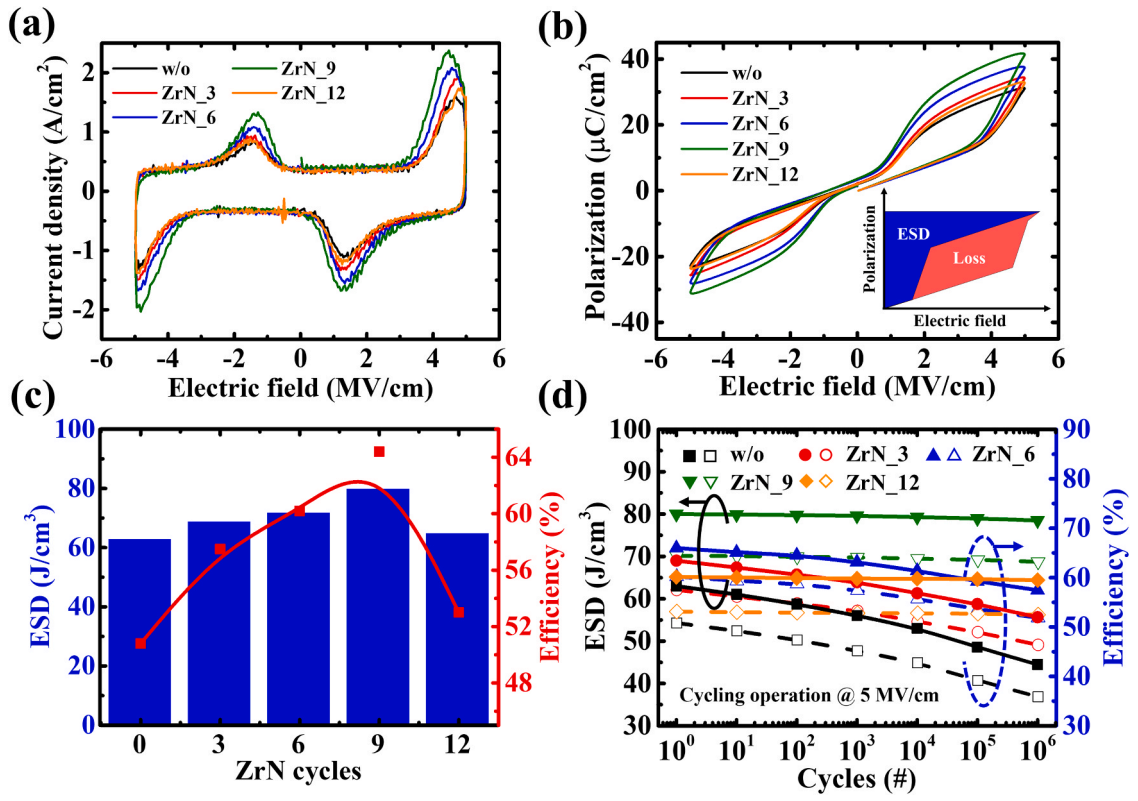

Fig. 4. (a) *J–E* and (b) *P–E* curves of TiN/ZrO_2/TiN MIM capacitors with different ALD cycles of ZrN interfacial layers. The inset shows the ESD and loss calculated from the integral of the blue and pink areas of *P–E* curves. (c) The values of ESD and efficiency of all samples obtained from *P–E* curves. (d) Cycling endurance characteristics of ESD and efficiency for TiN/ZrO_2/TiN MIM capacitors with different ALD cycles of ZrN interfacial layers.

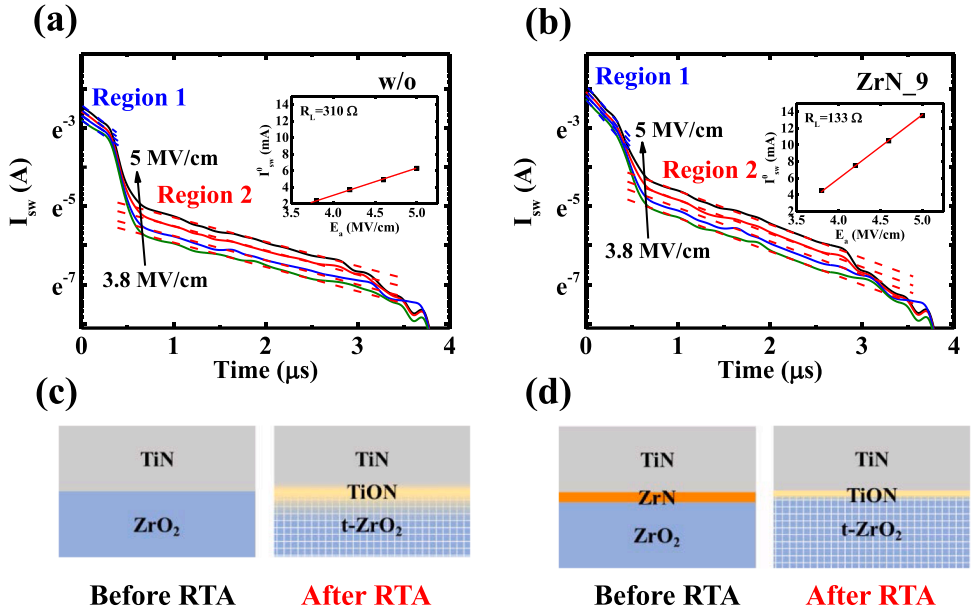

Fig. 5. $I_{sw}-t$ curves measured at different electric fields of TiN/ZrO_2/TiN MIM capacitors (a) without and (b) with a ZrN interfacial layer of 9 cycles. The inset shows $I^0_{SW}-E_a$ curves to extract R_L and E_c. Schematics of the interface between the ZrO_2 thin films and TiN electrode of the samples (c) without and (d) with a ZrN interfacial layer of 9 cycles.

samples measured at elevated temperatures were performed. However, the high temperature measurement at high electric field would induce a severe leakage current, as shown in Fig. S10, hindering the EC effect [49]. Thus, the maximum electric field for the polarization measurement was reduced from 5 to 4.5 MV/cm. Fig. 6a and Fig. S11 show the $P-E$ hysteresis curves of the TiN/ZrO_2/TiN MIM capacitors with different thicknesses of ZrN interfacial layer measured from 298 K to 388 K to investigate the EC effect. Meanwhile, the temperature dependence on the energy storage performance was examined, as shown in Fig. S12. It can be found that there is no significant trending in energy storage

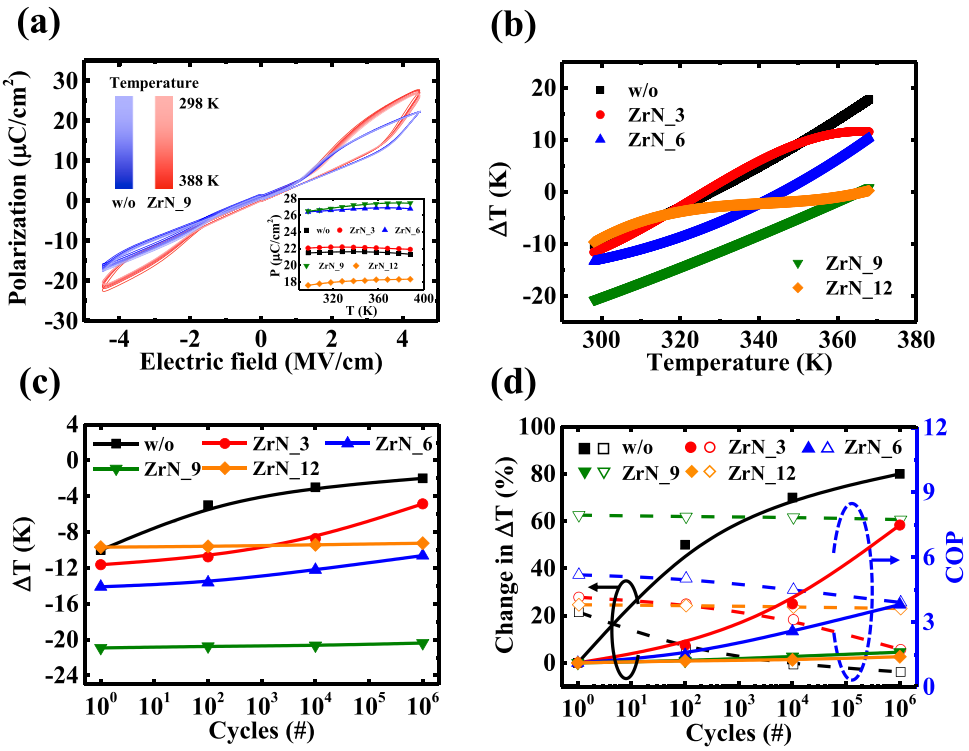

Fig. 6. (a) *P–E* curves of TiN/ZrO_2/TiN MIM capacitors without and with a ZrN interfacial layer of 9 cycles at temperatures ranging from 298 K to 388 K. The insets show the *P–T* curves of all samples as the function of temperature estimated from 298 K to 388 K. (b) ΔT of all samples as the function of temperature estimated from 298 K to 388 K. (c) ΔT and (d) change in ΔT and COP of all samples under different numbers of cycling endurance tests.

performance as a function of temperature, suitable for the extraction of adiabatic temperature change of the AFE ZrO_2 thin films. According to the Maxwell's equations, the EC effect can be obtained indirectly via the following formula:

$$\Delta T = -\frac{T}{\rho C_p}\int_{E_1}^{E_2}\left(\frac{\partial P}{\partial T}\right)_E dE \quad (5)$$

where ρ and C_p are the density and specific heat capacity of the ZrO_2 thin films, respectively [50,51]. To obtain the numerical differentiation of $\partial P/\partial T$, the polarization versus temperature ($P-T$) characteristics were plotted and fitted using a fourth-order polynomial, as shown in the inset of Fig. 6a. Then, the ΔT of all samples at different temperatures was calculated via Eq. (5) and is shown in Fig. 6b. It can be observed that the ZrN_9 sample exhibited a negative EC effect for all the measurement temperatures and an enhanced ΔT of -21 K was obtained under 4.5 MV/cm at 298 K, corresponding to the largest polarized response with the change in temperature at room temperature. However, at high temperature, a positive EC effect was observed in the samples with a ZrN interfacial layer of less than 9 cycles because of the low energy barrier for the change between the non-polar and polar phases [52]. Moreover, the cycling endurance tests of the ΔT under 4.5 MV/cm at 298 K for 10^6 cycles were performed and are presented in Fig. 6c. The EC effects of all samples measured from 298 K to 388 K after different cycles of endurance test were examined and are showed in Figs. S13–S16. When the thickness of the ZrN interfacial layer increased, the stability of EC effect was significantly improved owing to the suppressed interfacial dead layer as revealed in Fig. 5. To quantify the improvement of the cooling efficiency under the cycling operation, the change in ΔT and the coefficient of performance (COP) were calculated and are presented in Fig. 6d. The COP can be calculated via $|Q|/W_{total}$, where Q is $T \times \Delta S$ and W_{total} is the integral of the electric field with respect to the polarization in $P-E$ hysteresis curves of Fig. 6a, Fig. S11, and Figs. S13–S15. Additionally, the ΔS is equal to $\Delta T \times C_p/T$. For the ZrN_9 sample, the COP was found to be 7.9 and 7.4 before and after the cycling endurance tests of 10^6 cycles, respectively, which were the largest as compared with others. Fig. 7 shows the benchmarks of the cycling endurance characteristics after the tests of 10^6 cycles in energy storage and EC effect of this study and other literatures [15,53–66]. With a high ESD value of more than 80 J/cm^3, the changes in ESD and efficiency after the cycling endurance tests of 10^6 cycles of the AFE ZrO_2 capacitors with a ZrN interfacial layer of 9 cycles are comparable to those of other works, as presented in Fig. 7a,b. Furthermore, the highest absolute value of ΔT with a low change in ΔT after the cycling endurance tests of 10^6 cycles was obtained in this study, as shown in Fig. 7c, indicating that the TiN/ZrO_2/TiN MIM capacitors with a ZrN interfacial layer are suitable for the device cooling in ICs.

4. Conclusion

In summary, the TiN/ZrO_2/TiN MIM capacitors with ZrN as the interfacial layer were demonstrated to suppress the redox reaction between the TiN TE and ZrO_2 thin films and enhance the AFE and EC behaviors. With an increase in ALD cycles of the ZrN interfacial layer, the ESD and efficiency of the ZrO_2 capacitors were significantly increased to 80.2 J/cm^3 and 64.2 %, respectively, indicating the more polarized domains in ZrO_2 thin films, as confirmed in the HAADF images. Through the extraction of the interfacial capacitance, the interfacial dead layer of the samples with a ZrN interfacial layer was effectively reduced, corresponding to the less non-polar ZrO_2 at the interface. Furthermore, the cycling endurance stability of energy storage characteristics was improved because of the suppression of oxygen vacancy generation during the cycling operation. The TiN/ZrO_2/TiN MIM capacitors with a ZrN interfacial layer of 9 cycles exhibited a competitive ΔT of -21 K at 298 K and a negligible change in ΔT of 4.5 % after a cycling endurance test of 10^6 cycles. Based on the improvement in energy storage and EC behaviors as well as the robust reliability, the ZrN interfacial layer was suggested to be highly promising in AFE ZrO_2-based devices for energy storage in supercapacitors and solid-state

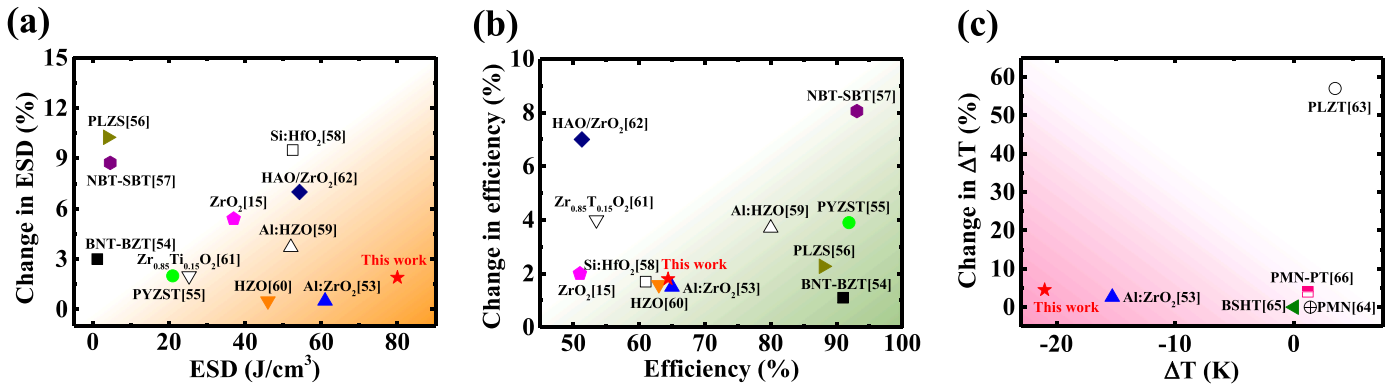

Fig. 7. Benchmarks of cycling endurance characteristics after the tests of 10^6 cycles in (a) ESD, (b) efficiency, and (c) EC effect of the TiN/ZrO_2/TiN MIM capacitor with a ZrN interfacial layer of 9 cycles and other studies.

cooling in ICs.

CRediT authorship contribution statement

Yu-Hua Liu: Investigation, Validation, Data curation, Writing – original draft. **Han-Hsiang Tai:** Investigation, Validation. **Chi-An Ho:** Investigation. **Ting-Han Lin:** Investigation. **Ming-Chung Wu:** Methodology, Validation. **Jer-Chyi Wang:** Conceptualization, Methodology, Writing – review & editing, Supervision.

Declaration of Competing Interest

The authors declare that they have no known competing financial interests or personal relationships that could have appeared to influence the work reported in this paper.

Acknowledgements

This research was supported by National Science and Technology Council, R.O.C. (Contract Nos. of NSTC 110-2221-E-182-058, NSTC 111-2221-E-182–062, and NSTC 111-2119-M-492-001-MBK) and Chang Gung Memorial Hospital, Linkou, Taiwan (Contract Nos. of CMRPD2M0101, CMRPD2M0281, and BMRPA74). The authors would like to thank the Microscopy Center at Chang Gung University for technical assistance.

Appendix A. Supporting information

Supplementary data associated with this article can be found in the online version at doi:10.1016/j.jeurceramsoc.2023.08.051.

References

[1] M.H. Park, H.J. Kim, Y.J. Kim, T. Moon, K. Do Kim, C.S. Hwang, Toward a multifunctional monolithic device based on pyroelectricity and the electrocaloric effect of thin antiferroelectric $Hf_xZr_{1-x}O_2$ films, Nano Energy 12 (2015) 131–140, https://doi.org/10.1016/j.nanoen.2014.09.025.
[2] Digitaltrends: Trending in Computing. ⟨https://www.digitaltrends.com/computing/amd-predicts-gpus-with-700-watt-tdp-by-2025/⟩.
[3] M. Valant, Electrocaloric materials for future solid-state refrigeration technologies, Prog. Mater. Sci. 57 (2012) 980–1009, https://doi.org/10.1016/j.pmatsci.2012.02.001.
[4] J.G. Webster, Z. Kutnjak, B. Rožič, R. Pirc, Electrocaloric effect: theory, measurements, and applications, Wiley Encycl. Electr. Electron. Eng. (2015) 1–19, https://doi.org/10.1002/047134608x.w8244.
[5] J.F. Scott, Electrocaloric materials, Annu. Rev. Mater. Res. 41 (2011) 229–240, https://doi.org/10.1146/annurev-matsci-062910-100341.
[6] I. Ponomareva, S. Lisenkov, Bridging the macroscopic and atomistic descriptions of the electrocaloric effect, Phys. Rev. Lett. 108 (2012) 1–5, https://doi.org/10.1103/PhysRevLett.108.167604.
[7] F.L. Goupil, A. Berenov, A.-K. Axelsson, M. Valant, N.McN. Alford, Direct and indirect electrocaloric measurements on⟨001⟩–$PbMg_{1/3}Nb_{2/3}O_3$-30$PbTiO_3$ single crysta, J. Appl. Phys. 111 (2012) 124109–124116, https://doi.org/10.1063/1.4730338.
[8] Y. Liu, J.F. Scott, B. Dkhil, Direct and indirect measurements on electrocaloric effect: recent developments and perspectives, Appl. Phys. Rev. 3 (2016), 031102, https://doi.org/10.1063/1.4958327.
[9] B. Neese, B. Chu, S.-G. Lu, Y. Wang, E. Furman, Q.M. Zhang, Large electrocaloric effect in ferroelectric polymers near room temperature, Science 321 (2008) 821–823, https://doi.org/10.1126/science.1159655.
[10] A.S. Mischenko, Q. Zhang, J.F. Scott, R.W. Whatmore, N.D. Mathur, Giant electrocaloric effect in thin-film $PbZr_{0.95}Ti_{0.05}O_3$, Science 37 (2006) 1270–1272, https://doi.org/10.1126/science.1123811.
[11] M.H. Park, H.J. Kim, Y.J. Kim, T. Moon, K. Do Kim, Y.H. Lee, S.D. Hyun, C. S. Hwang, Giant negative electrocaloric effects of $Hf_{0.5}Zr_{0.5}O_2$ thin films, Adv. Mater. 28 (2016) 7956–7961, https://doi.org/10.1002/adma.201602787.
[12] S. Pandya, G. Velarde, L. Zhang, L.W. Martin, Pyroelectric and electrocaloric effects in ferroelectric silicon-doped hafnium oxide thin films, Phys. Rev. Mater. 2 (2018), 124405, https://doi.org/10.1103/PhysRevMaterials.2.124405.
[13] B. Allouche, H.J. Hwang, T.J. Yoo, B.H. Lee, A negative electrocaloric effect in an antiferroelectric zirconium dioxide thin film, Nanoscale 12 (2020) 3894–3901, https://doi.org/10.1039/c9nr07293d.
[14] S.E. Reyes-Lillo, K.F. Garrity, K.M. Rabe, Antiferroelectricity in thin-film ZrO_2 from first principles, Phys. Rev. B 90 (2014), 140103, https://doi.org/10.1103/PhysRevB.90.140103.
[15] M. Pešić, M. Hoffmann, C. Richter, T. Mikolajick, U. Schroeder, Nonvolatile random access memory and energy storage based on antiferroelectric like hysteresis in ZrO_2, Adv. Funct. Mater. 26 (2016) 7486–7494, https://doi.org/10.1002/adfm.201603182.
[16] M.H. Park, H.J. Kim, Y.J. Kim, W. Jeon, Taehwan Moon, C.S. Hwang, Ferroelectric properties and switching endurance of $Hf_{0.5}Zr_{0.5}O_2$ films on TiN bottom and TiN or RuO_2 top electrodes, Phys. Status Solidi RRL 8 (2014) 532, https://doi.org/10.1002/pssr.201409017.
[17] J.P.B. Silva, K.C. Sekhar, H. Pan, J.L. MacManus-Driscoll, M. Pereira, Advances in dielectric thin films for energy storage applications, revealing the promise of group IV binary oxides, ACS Energy Lett. 6 (2021) 2208–2217, https://doi.org/10.1021/acsenergylett.1c00313.
[18] B.Y. Kim, H.W. Park, S.D. Hyun, Y.B. Lee, S.H. Lee, M. Oh, S.K. Ryoo, I.S. Lee, S. Byun, D. Shim, D.Y. Cho, M.H. Park, C.S. Hwang, Enhanced ferroelectric properties in $Hf_{0.5}Zr_{0.5}O_2$ films using a $HfO_{0.61}N_{0.72}$ interfacial layer, Adv. Electron. Mater. 8 (2021) 2100042, https://doi.org/10.1002/aelm.202100042.
[19] K.Y. Chen, P.H. Chen, R.W. Kao, Y.X. Lin, Y.H. Wu, Impact of plasma treatment on reliability performance for $HfZrO_x$-based metal-ferroelectric-metal capacitors, IEEE Electron Device Lett. 39 (2018) 87–90, https://doi.org/10.1109/LED.2017.2771390.
[20] N. Golshani, V. Mohammadi, H. Schellevis, C.I.M. Beenakker, R. Ishihara, Research update: reactively sputtered nanometer-thin ZrN film as a diffusion barrier between Al and boron layers for radiation detector applications, APL Mater. 2 (2014), 100702, https://doi.org/10.1063/1.4897959.
[21] F. Khatkhatay, J. Jian, L. Jiao, Q. Su, J. Gan, J.I. Cole, H. Wang, Diffusion barrier properties of nitride-based coatings on fuel cladding, J. Alloy. Compd. 5 (2013) 442–448, https://doi.org/10.1016/j.jallcom.2013.06.108.
[22] Y. Yuan, J. Wang, S. Adimi, H. Shen, T. Thomas, R. Ma, J.P. Attfield, M. Yang, Zirconium nitride catalysts surpass platinum for oxygen reduction, Nat. Mater. 19 (2020) 282–286, https://doi.org/10.1038/s41563-019-0535-9.
[23] D.D. Kumar, G.S. Kaliaraj, Multifunctional zirconium nitride/copper multilayer coatings on medical grade 316L SS and titanium substrates for biomedical applications, J. Mech. Behav. Biomed. Mater. 77 (2018) 106–115, https://doi.org/10.1016/j.jmbbm.2017.09.007.
[24] G. Brunello, P. Brun, C. Gardin, L. Ferroni, E. Bressan, R. Meneghello, B. Zavan, S. Sivolella, Biocompatibility and antibacterial properties of zirconium nitride coating on titanium abutments: an in vitro study, PLoS One 13 (2018), e0199591, https://doi.org/10.1371/journal.pone.0199591.
[25] C. Sleigh, A.P. Pijpers, A. Jaspers, B. Coussens, R.J. Meier, On the determination of atomic charge via ESCA including application to organometallics, J. Electron.

Spectrosc. Relat. Phenom. 77 (1996) 41–57, https://doi.org/10.1016/0368-2048(95)02392-5.
[26] M. Chen, X. Wang, Y.H. Yu, Z.L. Pei, X.D. Bai, C. Sun, R.F. Huang, L.S. Wen, X-ray photoelectron spectroscopy and auger electron spectroscopy studies of Al-doped ZnO films, Appl. Surf. Sci. 158 (2000) 134–140, https://doi.org/10.1016/S0169-4332(99)00601-7.
[27] C.S. Lee, C.H. Jeon, B.T. Lee, S.H. Jeong, Abrupt conversion of the conductivity and band-gap in the sputter grown Ga-doped ZnO films by a change in growth ambient: effects of oxygen partial pressure, J. Alloy. Compd. 742 (2018) 977–985, https://doi.org/10.1016/j.jallcom.2018.01.351.
[28] A.R. González-Elipe, G. Munuera, J.P. Espinos, J.M. Sanz, Compositional changes induced by 3.5 keV Ar^+ ion bombardment in Ni-Ti oxide systems: a comparative study, Surf. Sci. 220 (1989) 368–380, https://doi.org/10.1016/0039-6028(89)90239-2.
[29] A.R. Chourasia, D.R. Chopra, X-ray photoelectron study of TiN, Surf. Sci. Spectra 1 (1992) 233–237, https://doi.org/10.1116/1.1247644.
[30] C.E. Myers, H.F. Franzen, J.W. Anderegg, X-ray photoelectron spectra and bonding in transition-metal phosphides, Inorg. Chem. 24 (1985) 1822–1824, https://doi.org/10.1021/ic00206a025.
[31] S. Sinha, S. Badrinarayanan, A.P.B. Sinha, Interaction of oxygen with $Zr_{76}Fe_{24}$ metglass: an X-ray photoelectron spectroscopy study, J. Less Common Met. 125 (1986) 85–95, https://doi.org/10.1016/0022-5088(86)90082-2.
[32] Y.E. Ke, Y.I. Chen, Effects of nitrogen flow ratio on structures, bonding characteristics, and mechanical properties of ZrN_x films, Coatings 10 (2020) 476, https://doi.org/10.3390/coatings10050476.
[33] I. Milošev, H.H. Strehblow, M. Gaberšček, B. Navinšek, Electrochemical oxidation of ZrN hard (PVD) coatings studied by XPS, Surf. Interface Anal. 24 (1996) 448–458, https://doi.org/10.1002/(SICI)1096-9918(199607)24:7<448::AID-SIA137>3.0.CO;2-F.
[34] H. Ikawa, T. Yamada, K. Kojima, S. Matsumoto, X-ray photoelectron spectroscopy study of high- and low-temperature forms of zirconium titanate, J. Am. Ceram. Soc. 74 (1991) 1459–1462, https://doi.org/10.1111/j.1151-2916.1991.tb04131.x.
[35] J. Málek, L. Beneš, T. Mitsuhashi, Powder diffraction data and Rietveld refinement of metastable t-ZrO_2 at low temperature, Powder Diffr. 12 (1997) 96–98, https://doi.org/10.1017/S0885715600009519.
[36] P.D. Lomenzo, M. Materano, T. Mittmann, P. Buragohain, A. Gruverman, T. Kiguchi, T. Mikolajick, U. Schroeder, Harnessing phase transitions in antiferroelectric ZrO_2 using the size effect, Adv. Electron. Mater. 8 (2022), 2100556, https://doi.org/10.1002/aelm.202100556.
[37] Y. Lee, Y. Goh, J. Hwang, D. Das, S. Jeon, The influence of top and bottom metal electrodes on ferroelectricity of hafnia, IEEE Trans. Electron Devices 68 (2021) 523–528, https://doi.org/10.1109/TED.2020.3046173.
[38] C.H. Choi, T.S. Jeon, R. Clark, D.L. Kwong, Electrical properties and thermal stability of CVD HfO_xN_y gate dielectric with poly-Si gate electrode, IEEE Electron Device Lett. 24 (2003) 215–217, https://doi.org/10.1109/LED.2003.810881.
[39] W.E. Fu, Y.Q. Chang, Y.C. Chen, Post-deposition annealing analysis for HfO_2 thin films using GIXRR/GIXRD, AIP Conf. Proc. 1173 (2009) 122–126, https://doi.org/10.1063/1.3251205.
[40] C.Y. Wang, C.I. Wang, S.H. Yi, T.J. Chang, C.Y. Chou, Y.T. Yin, M. Shiojiri, M. J. Chen, Paraelectric/antiferroelectric/ferroelectric phase transformation in As-deposited ZrO_2 thin films by the TiN capping engineering, Mater. Des. 195 (2020), 109020, https://doi.org/10.1016/j.matdes.2020.109020.
[41] M.G. Kozodaev, A., G. Chernikova, R.R. Khakimov, M.H. Park, A.M. Markeev, C. S. Hwang, La-doped $Hf_{0.5}Zr_{0.5}O_2$ thin films for high-efficiency electrostatic supercapacitors, Appl. Phys. Lett. 113 (2018), 123902, https://doi.org/10.1016/0368-2048(95)02392-5.
[42] X. Lyu , M. Si , X. Sun , M.A. Capano , H. Wang , P.D. Ye , Ferroelectric and anti-ferroelectric hafnium zirconium oxide: Scaling limit, switching speed and record high polarization density, in: Proceedings of the Dig. Tech. Pap. - Symp. VLSI Technol. 2019-June (2019) T44–T45. https://doi.org/10.23919/VLSIT.2019.8776548.
[43] R. Meyer, R. Waser, K. Prume, T. Schmitz, S. Tiedke, Dynamic leakage current compensation in ferroelectric thin-film capacitor structures, Appl. Phys. Lett. 86 (2005) 1–3, https://doi.org/10.1063/1.1897425.
[44] M. Guo, B. Sun, M. Wu, H. Sun, L. Zhang, Q. Liu, D. Wang, X. Lou, Effect of polarization fatigue on the electrocaloric effect of relaxor $Pb_{0.92}La_{0.08}Zr_{0.65}Ti_{0.35}O_3$ thin film, Appl. Phys. Lett. 117 (2020), 202901, https://doi.org/10.1063/5.0018741.
[45] N. Umezawa, K. Shiraishi, T. Ohno, H. Watanabe, T. Chikyow, K. Torii, K. Yamabe, K. Yamada, H. Kitajima, T. Arikado, First-principles studies of the intrinsic effect of nitrogen atoms on reduction in gate leakage current through Hf-based high-k dielectrics, Appl. Phys. Lett. 86 (2005), 143507, https://doi.org/10.1063/1.1899232.
[46] X.Y. Zhao, J.P. Xu, L. Liu, Z. Li, Improved electrical properties of top-gate MoS_2 transistor with NH_3-plasma treated HfO_2 as gate dielectric, IEEE Electron. Device Lett. 41 (2020) 385–388, https://doi.org/10.1109/LED.2020.3013069.
[47] M.H. Park, H.J. Kim, Y.H. Lee, Y.J. Kim, T. Moon, K. Do Kim, S.D. Hyun, C. S. Hwang, Two-step polarization switching mediated by a nonpolar intermediate phase in $Hf_{0.4}Zr_{0.6}O_2$ thin films, Nanoscale 8 (2016) 13898–13907, https://doi.org/10.1039/C5NR08346J.
[48] A.Q. Jiang, H.J. Lee, C.S. Hwang, T.A. Tang, Resolving the Landauer paradox in ferroelectric switching by high-field charge injection, Phys. Rev. B 80 (2009), 024119, https://doi.org/10.1103/PhysRevB.80.024119.
[49] B. Peng, H. Fan, Q. Zhang, A giant electrocaloric effect in nanoscale antiferroelectric and ferroelectric phases coexisting in a relaxor $Pb_{0.8}Ba_{0.2}ZrO_3$ thin film at room temperature, Adv. Funct. Mater. 23 (2013) 2987–2992, https://doi.org/10.1002/adfm.201202525.
[50] S. Di Mo, W.Y. Ching, Electronic and optical properties of three phases of titanium dioxide: rutile, anatase, and brookite, Phys. Rev. B 51 (1995) 13023–13032, https://doi.org/10.1103/PhysRevB.51.13023.
[51] X. Luo, W. Zhou, S.V. Ushakov, A. Navrotsky, A.A. Demkov, Monoclinic to tetragonal transformations in hafnia and zirconia: a combined calorimetric and density functional study, Phys. Rev. B Condens. Matter Mater. Phys. 80 (2009) 1–13, https://doi.org/10.1103/PhysRevB.80.134119.
[52] N. Liu, R. Liang, G. Zhang, Z. Zhou, S. Yan, X. Li, X. Dong, Colossal negative electrocaloric effects in lead-free bismuth ferrite-based bulk ferroelectric perovskite for solid-state refrigeration, J. Mater. Chem. C 6 (2018) 10415–10421, https://doi.org/10.1039/C8TC04125C.
[53] Y.H. Liu, L.H. Lin, S.H. Lu, H.C. Lu, J.C. Wang, Highly reliable electrocaloric behaviors of antiferroelectric Al:ZrO_2 thin films for solid-state cooling in integrated circuits, IEEE Trans. Electron Devices 68 (2021) 6352–6358, https://doi.org/10.1109/TED.2021.3119532.
[54] Y. Huang, F. Li, H. Hao, F. Xia, H. Liu, S. Zhang, $(Bi_{0.51}Na_{0.47})TiO_3$ based lead free ceramics with high energy density and efficiency, J. Mater. 5 (2019) 385–393, https://doi.org/10.1016/j.jmat.2019.03.006.
[55] C.W. Ahn, G. Amarsanaa, S.S. Won, S.A. Chae, D.S. Lee, I.W. Kim, Antiferroelectric thin-film capacitors with high energy-storage densities, low energy losses, and fast discharge times, ACS Appl. Mater. Interfaces 7 (2015) 26381–26386, https://doi.org/10.1021/acsami.5b08786.
[56] X. Liu, Y. Li, N. Sun, X. Hao, High energy-storage performance of PLZS antiferroelectric multilayer ceramic capacitors, Inorg. Chem. Front. 7 (2020) 756–764, https://doi.org/10.1039/c9qi01416k.
[57] J. Li, F. Li, Z. Xu, S. Zhang, Multilayer lead-free ceramic capacitors with ultrahigh energy density and efficiency, Adv. Mater. 30 (2018), 1802155, https://doi.org/10.1002/adma.201802155.
[58] F. Ali, X. Liu, D. Zhou, X. Yang, J. Xu, T. Schenk, J. Müller, U. Schroeder, F. Cao, X. Dong, Silicon-doped hafnium oxide anti-ferroelectric thin films for energy storage, J. Appl. Phys. 122 (2017), 144105, https://doi.org/10.1063/1.4989908.
[59] P.D. Lomenzo, C.C. Chung, C. Zhou, J.L. Jones, T. Nishida, Doped $Hf_{0.5}Zr_{0.5}O_2$ for high efficiency integrated supercapacitors, Appl. Phys. Lett. 110 (2017), 232904, https://doi.org/10.1063/1.4985297.
[60] K.D. Kim, Y.H. Lee, T. Gwon, Y.J. Kim, H.J. Kim, T. Moon, S.D. Hyun, H.W. Park, M.H. Park, C.S. Hwang, Scale-up and optimization of HfO_2-ZrO_2 solid solution thin films for the electrostatic supercapacitors, Nano Energy 39 (2017) 390–399, https://doi.org/10.1016/j.nanoen.2017.07.017.
[61] Y.H. Liu, P.C. Wang, L.H. Lin, J.C. Wang, Antiferroelectric titanium-doped zirconia thin films deposited via HiPIMS for highly efficient electrocaloric applications, J. Eur. Ceram. Soc. 41 (2021) 3387–3396, https://doi.org/10.1016/j.jeurceramsoc.2020.12.041.
[62] J.P.B. Silva, J.M.B. Silva, K.C. Sekhar, H. Palneedi, M.C. Istrate, R.F. Negrea, C. Ghica, A. Chahboun, M. Pereiraa, M.J.M. Gomes, Energy storage performance of ferroelectric ZrO_2 film capacitors: effect of HfO_2:Al_2O_3 dielectric insert layer, J. Mater. Chem. A 8 (2020) 14171–14177, https://doi.org/10.1039/d0ta04984k.
[63] M. Guo, B. Sun, M. Wu, H. Sun, L. Zhang, Q. Liu, D. Wang, X. Lou, Effect of polarization fatigue on the electrocaloric effect of relaxor $Pb_{0.92}La_{0.08}Zr_{0.65}Ti_{0.35}O_3$thin film, Appl. Phys. Lett. 117 (2020), 202901, https://doi.org/10.1063/5.0018741.
[64] A. Bradeško, L. Fulanović, M. Vrabelj, M. Otoničar, H. Uršič, A. Henriques, C. C. Chung, J.L. Jones, B. Malič, Z. Kutnjak, T. Rojac, Electrocaloric fatigue of lead magnesium niobate mediated by an electric-field-induced phase transformation, Acta Mater. 169 (2019) 275–283, https://doi.org/10.1016/j.actamat.2019.03.017.
[65] J. Li, J. Lv, D. Zhang, L. Zhang, X. Hao, M. Wu, B.X. Xu, M. Otonicar, T. Lookman, B. Dkhil, X. Lou, Doping-induced polar defects improve the electrocaloric performance of $Ba_{0.9}Sr_{0.1}Hf_{0.1}Ti_{0.9}O_3$, Phys. Rev. Appl. 16 (2021), 014033, https://doi.org/10.1103/PhysRevApplied.16.014033.
[66] M.G. Del Duca, J. Tušek, A. Maiorino, L. Fulanović, A. Bradeško, U. Plaznik, B. Malič, C. Aprea, A. Kitanovski, Comprehensive evaluation of electrocaloric effect and fatigue behavior in the $0.9Pb(Mg_{1/3}Nb_{2/3})O_3$-$0.1PbTiO_3$ bulk relaxor ferroelectric ceramic, J. Appl. Phys. 128 (2020), 104102, https://doi.org/10.1063/5.0003250.